A simulated microgravity biofilm reactor with integrated microfabricated sensors: Advancing biofilm studies in near-space conditions

Haley M. Ketteler; Erick L. Johnson; Matthew McGlennen; Markus Dieser; Christine M. Foreman; Stephan Warnat

Biofilm 9 (2025) 100263

Contents lists available at ScienceDirect

Biofilm

journal homepage: www.sciencedirect.com/journal/biofilm

A simulated microgravity biofilm reactor with integrated microfabricated sensors: Advancing biofilm studies in near-space conditions

Haley M. Ketteler [a,b,c], Erick L. Johnson [c], Matthew McGlennen [a,c], Markus Dieser [a,d], Christine M. Foreman [a,d], Stephan Warnat [a,c,*]

[a] Center for Biofilm Engineering, Montana State University, Bozeman, MT, USA
[b] Electrical and Computer Engineering, Montana State University, Bozeman, MT, USA
[c] Mechanical and Industrial Engineering, Montana State University, Bozeman, MT, USA
[d] Chemical and Biological Engineering, Montana State University, Bozeman, MT, USA

ARTICLE INFO

Keywords:
Simulated microgravity
Rotating wall vessel
Low shear stress
Biofilm
Space
Microfabricated sensor

ABSTRACT

Studying biofilms in a microgravity environment currently relies on one of two scenarios, collecting planktonic aggregates in rotating wall vessels or performing experiments in the microgravity environment of space on the International Space Station. While informative techniques, both have their limitations when studying surface-attached microbial communities. A simulated microgravity biofilm reactor (SMBR) was developed to study biofilms in microgravity, coupled with the integration of microfabricated sensors for internal system monitoring. The establishment of simulated microgravity was demonstrated through computational fluid dynamic modelling revealing low fluid shear stress conditions (<1 mPa) throughout the reactor and on the wall surface. Microfabricated resistance temperature devices integrated in the reactor walls confirmed the capability for continuous sensor measurements during operation with the ability to perform traditional microbiology analyses on the sensor surface following an experiment. Microbiological analyses established that there were no significant differences in biofilm growth between sensor and wall surfaces within the reactor. With the integration of defined sampling surfaces, the SMBR allows for in-depth biofilm analysis in a repeatable and accessible manner allowing for a greater understanding of the effects of microgravity on biofilm.

1. Introduction

Biofilms are defined as surface-adherent accumulations of microorganisms embedded in an extracellular polymeric substance [1]. Biofilm formation and dispersal can cause corrosion of surfaces and critical blockage of pipes, ultimately affecting water quality, raising health concerns, and leading to operational and mechanical failure. Such biofilm related issues become particularly problematic where maintenance is impractical due to limited resupply capabilities. One such example is biofilm formation within the Environmental Control and Life Support Systems (ECLSS) of the International Space Station (ISS) and the former Russian Mir station; both setting an important precedent for the pervasiveness of biofilms in manned spacecraft and the risk biofilms may pose to the health of crew members and the spacecraft [2–4]. Currently, biofilm management on the ISS is achieved by biocide dosing, periodic component replacement, and water testing [4–6]. While this is a feasible approach for low Earth orbit (LEO) missions, there are several limitations for future destinations. As mission durations increase and life support systems experience dormant periods lasting months to years, maintaining optimal performance is critical for the success of Mars and Moon exploration.

Microgravity, a condition where the force of gravity is balanced by inertial forces, is believed to significantly affect biological systems in space environments [7,8]. While much needs to be learned about the effects of microgravity on microbes, experiments on the ISS have suggested that microgravity can affect microbial gene expression, cell morphology, physiology, virulence, and biofilm formation [9–15]. For instance, biofilm grown under microgravity conditions exhibited increased viability, biomass, thickness, and antibiotic resistance compared to normal Earth gravity controls [11,16]. Due to the logistical limitations of research in space, ground-based analogs are necessary to explore the effect of microgravity on biofilm.

The spaceflight environment is characterized by the reduction of gravity, which prevents sedimentation or buoyancy-driven convection.

* Corresponding author. Center for Biofilm Engineering, Montana State University, Bozeman, MT, USA.
E-mail address: stephan.warnat@montana.edu (S. Warnat).

https://doi.org/10.1016/j.bioflm.2025.100263
Received 20 November 2024; Received in revised form 29 January 2025; Accepted 16 February 2025
Available online 17 February 2025

Low shear modelled microgravity (LSMMG) has emerged as an analog to emulate aspects of the microgravity environment experienced in space (i.e., low fluid shear and non-unidirectional gravity) and can be generated using a 2D clinostat or rotating wall vessel (RWV) [17–20]. Historically, the fluid behavior of simulated microgravity has been defined as fluid shear forces below 92 mPa [21]. These fluid shear levels were originally established for mammalian cells; however, it is well known that bacterial cells respond differently to shear [22]. More recently, low shear in simulated microgravity environments has been redefined to be 1 mPa or less [23–25].

To address the non-unidirectional gravity of spaceflight, the RWV is designed to best simulate the microgravity environment at the center of rotation [8,26]. By rotating the reactor at a speed corresponding to the terminal velocity of a particle, the particles will remain suspended. The generally accepted range of rotation speeds for microbiology applications is 5–30 RPM; however, individual cells may aggregate. Larger aggregates will drift to the wall of the reactor due to the combination of forces acting on the aggregate (i.e. centrifugal, Coriolis, and buoyant forces) [8,17,27]. Ultimately, the transition from a suspended particle to a wall-fixed particle terminates the conventional model of the simulated microgravity environment. As biofilms are typically considered surface-attached colonies, understanding the environment at the wall of the reactor is integral to the determination of biofilm response in simulated microgravity. Considering two of the leading assumptions of microgravity (i.e., low fluid shear and non-unidirectional gravity), an extension of the simulated microgravity environment to the walls of the reactor could be warranted for biofilm research.

Studying biofilms in space comes with a myriad of challenges. One shortcoming of traditional microbiology for space applications is the time delay in detecting contamination [28]. As detailed in sections TX06.1.5 and TX06.4.1 of the 2020 NASA Technology Roadmap, methods for microbial detection that limit required crew time and material usage are needed for future crewed space missions [29]. Promising solutions for the real-time detection of bacterial activity and biofilm growth include optical imaging sensors, micro-interdigitated electrode impedance sensors, and quartz crystal microbalance sensors [30–32]. Due to the complexities of electrical component integration in aqueous systems, sensors need to be integrated at the pipe walls to minimize the introduction of flow patterns that may encourage biofilm growth and to minimize hardware complexity [33].

To better understand and control biofilm proliferation in space, this study developed a simulated microgravity biofilm reactor to investigate biofilm monitoring tools in a space relevant environment. The objectives of this study were to (*i*) develop a LSMMG reactor with sensor integration for continuous data collection, (*ii*) model the low-shear fluid environment inside the reactor to extend its application from planktonic to surface-attached biofilm studies, (*iii*) validate biofilm formation in a low shear fluid environment, and (*iv*) demonstrate sensor integration and measurements.

2. Methods and materials

2.1. Vessel design and fabrication

A benchtop Simulated Microgravity Biofilm Reactor (SMBR) was designed to grow biofilm on removable coupons and microfabricated sensors. The SMBR consists of two components: the SMBR body and the reactor base (Fig. 1). The reactor body consists of an 800 mL reaction chamber comprised of two 150 mm sections of polycarbonate tubing (2.75" I.D. (69.85 mm), McMaster Carr #8585K38) with a metallic coupon ring in the center and two metallic endcaps. The coupon ring was machined out of 6061 aluminum bar stock and features eight openings that house four microfabricated sensors and four biofilm coupons (Fig. 2). Sensors and coupons are exposed to the media through

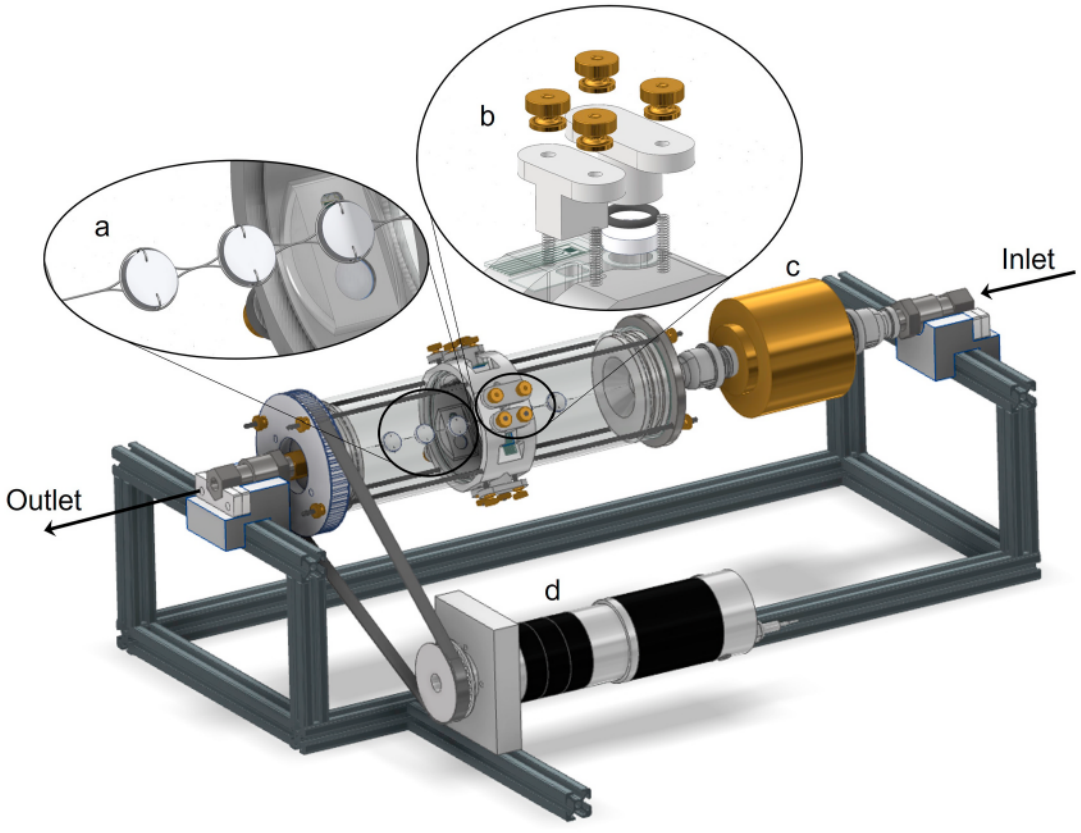

Fig. 1. CAD rendering of the Simulated Microgravity Biofilm Reactor (SMBR), with the main components indicated a) the centerline coupons, b) the sensor and biofilm coupon housing, c) the electrical slip ring, and d) the DC gearmotor. Also shown are the inlet and outlet used for filling and emptying the reactor.

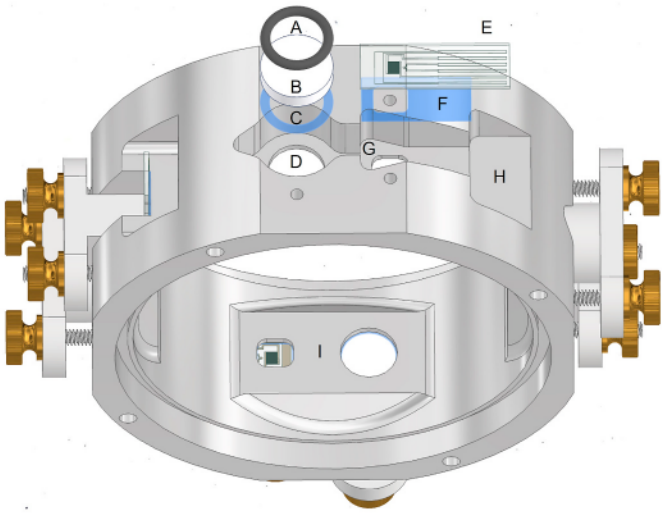

Fig. 2. CAD rendering of machined 6061 aluminum coupon ring with integrated sensors and biofilm coupons. The coupon/sensor integration assemblies are composed of A) O-ring to accommodate different coupon thicknesses, B) biofilm coupon, C) silicone gasket for a watertight seal with the biofilm coupon, D) biofilm coupon port, E) microfabricated sensor, F) silicone gasket for a watertight seal with the sensor, G) sensor port, H) card reader slot, and I) internal view of the sensor and biofilm coupon ports.

holes measuring 5.8 × 8.5 mm and 10 mm in diameter respectively, with a 1.27 mm recess (determined by manufacturing capabilities) (Fig. 2D and G). The reactor endcaps were machined from 6061 aluminum stock and achieve a watertight seal with the polycarbonate tubing using Buna-N O-rings (Buna-B, McMaster Carr #9452K152).

The coupon ring is fitted with four sensors and four biofilm coupons (0.1875" (4.76 mm) thick polypropylene, McMaster Carr #2898K12) and a watertight seal is achieved using custom cut silicone gaskets (0.01" (0.254 mm) thick, McMaster Carr #87315K61) and a 3D printed clamp (Fig. 1b). To test biofilm formation in the center of the reactor an additional set of six coupons is temporarily integrated along the centerline of the reactor and secured to the endcaps to allow for simultaneous rotation with the reactor body (Fig. 1a). A 150 mm long section of aluminum pipe (1" (25.4 mm) O.D.) is threaded into the influent endcap to accommodate an electrical slip ring (Moflon MT2586-P1210-VC) (Fig. 1c). Rotary joints (Mosmatic Rotary Union, DGV Swivel, NPTM x NPTF, ¼" (6.35 mm)) are connected to the aluminum pipe and the effluent endcap of the reactor to allow for fluid flow into the reactor during filling and operation. Plastic threaded barb adapters are used to connect the rotary joints to 4.8 mm I.D. silicone tubing (Masterflex #96400-25) at both the inlet and outlet (Fig. 1). Four threaded rods run the length of the reactor body to fasten the coupon ring, polycarbonate tubes, and endcaps together.

The reactor stand is assembled from aluminum T-slot rail (20 × 20 mm, McMaster Carr #5537T101) and supports the reactor at the rotary joints to allow for continuous rotation. The electrical slip ring (Fig. 1c) is attached to the aluminum rod and the stationary cables are secured to the reactor stand and then connected to the data logger (see temperature data collection). The reactor is driven by a DC gearmotor (Midwest Motion Products, #BL58-412D-24V GP52-100) via a timing belt (XL Series, 3/8" width, McMaster Carr #260XL037US) (Fig. 1d). A 60-tooth pulley (McMaster Carr #57105K33) is mounted to the effluent endcap, and a 30-tooth pulley (McMaster Carr #57105K25) is mounted on the motor shaft. The pulley ratio and motor rating allow for obtainable speeds from 1 to 24.8 RPM.

2.2. Computational fluid dynamics model of SMBR

The SMBR was modelled in the computational fluid dynamics (CFD) package Siemens Simcenter Star-CCM+ (v. 16.04.007) to estimate the scale of intra-fluid and wall shear stresses. A laminar and unsteady formulation was used to solve the coupled fluid equations. The SMBR was simulated from the influent rotary joint to the effluent rotary joint on the opposite end of the reactor with a constant angular velocity of $\omega = 24.8$ RPM around its central axis. An additional length of 100 mm of tubing was added to the fluid exit to account for the transition between rotating and non-rotating boundaries. The influent and effluent boundaries were specified as walls to approximate the batch mode conditions of the experiment without flow.

In the model, properties of water at room temperature were used, and water was treated as an incompressible, single-phase, Newtonian fluid. Gravity was not included, as it would only superimpose a hydrostatic pressure on top of the pressure gradient developed through rotation for this setup; however, if a multi-species fluid and/or particles with densities different than the carrying fluid are introduced, gravity would need to be included. A second-order time discretization was used with a time-step of 0.00667 s, resulting in 1° of rotation per time-step. Rigid-body rotation ($\boldsymbol{v} = 0\hat{r} + \omega r\hat{\theta} + 0\hat{z}$) was assumed for initial conditions to reduce the runtime. The model was run for 16.9361 s (7 revolutions) until the shear stress on the biofilm coupon and sensor surfaces reached an asymptotic value.

The SMBR was simulated as the full 3D geometry and as a ¼ symmetry model, split along the central axis to accommodate a mesh independence study [34]. A polyhedral mesh was generated within the inlet and outlet tubing, within the SMBR body, and on the biofilm coupon and sensor surfaces with an average element size of 500 μm, 150 μm, and 18.75 μm, respectively, for the most refined model. Additionally, the biofilm coupon and sensor surfaces had two prismatic layers to ensure uniform element thickness when calculating shear values. The remaining wall surfaces in the model (i.e. the polycarbonate tubing and coupon ring) had no additional mesh refinement. The total mesh count for the final, quartered simulation was 14,543,993 elements and the results presented are from this simulation. Reduced resolution simulations were analyzed to determine the impact of the centerline coupons on the bulk fluid velocity. The setup and results of these preliminary simulations can be found in the supplemental materials.

2.3. Sensor fabrication

To test the reliability of sensor integration in the SMBR, resistance temperature device (RTD) sensors on a multiparametric biosensor chip were used (Fig. 2e). The biosensor fabrication has been described previously [31]. A subset of the sensors (N = 6) was calibrated by recording resistance measurements of the RTDs at 15, 20, and 25 °C using a HIOKI RM3544-01 Resistance Meter connected to a Linkam temperature stage (Linkam Scientific Instruments #LTS420E-P). The thermal coefficient of resistance and reference resistance for each sensor was calculated and used to convert the sensor responses to temperature readings.

2.4. Cell culturing conditions

Ralstonia insidiosa, originally isolated from the International Space Station (Boeing isolate 19-597-yn-2), was used for all biofilm related experiments [35]. Cell culture enrichments were grown at 37 °C in 1X Tryptic Soy Broth (TSB) while shaking at 150 RPM for 24 h. Subsequently, enrichments were harvested at 10,000×*g* for 5 min, washed twice in phosphate-buffered saline (PBS), and transferred to 1:10X TSB. Enrichments were harvested at an optical density of $OD_{600} = 0.008$, resulting in a starting cell concentration in the reactors of ~5.6 $\log_{10}$ CFUs (colony-forming units) mL^{-1}.

2.5. SMBR experiment

Biofilm accumulation at the center of the reactor (i.e., the historically

accepted best approximation of microgravity) was compared to that at the wall surface where the sensors and biofilm coupons are located. Because the center coupons were integrated for biofilm comparison but are not intended to be a permanent component of the reactor, they were excluded from the CFD models presented herein. All SMBR components (reactor body, tubing, connectors, coupons, sensors, and gaskets) were autoclaved, followed by assembly in a Class II biological safety cabinet (Supplemental Figure S1). The reactor body was filled with sterile 1:10X TSB leaving no headspace and rotation was initiated (24.8 RPM). Once rigid body rotation conditions existed throughout the SMBR (~10 min), an 8 mL cell culture enrichment of *R. insidiosa* was injected aseptically through an injection port in the inlet tubing. This was followed by 50 mL of sterile 1:10X TSB to ensure the cells were predominantly located in the reactor body. The reactor was then run in batch mode for 24 h at ambient room temperature (22 ± 2.5 °C). Experiments were run in triplicate.

After 24 h of batch operation, the wall coupons and sensors were aseptically removed from the reactor and placed into individual 50 mL Falcon tubes containing 10 mL of 1X PBS solution and 10 μL of Tween 20 (0.1 % final concentration). A 1 mL sample of the bulk media was collected from the center of the reactor following removal of the first wall coupon. To retrieve the coupons from the centerline, the reactor was drained, and the coupons were immediately removed and placed into individual Falcon tubes. The Falcon tubes were vortexed for 1 min. CFU enumeration was carried out using drop plating on Tryptic Soy agar followed by incubation at 22 °C for 96 h.

The biofilm CFUs were normalized to the exposed surface area for each sampling location and transformed to log densities. A linear mixed effects model was applied to the biofilm data with a random effect for the reactor and a fixed effect for the sampling location. A Tukey test with 90 % confidence intervals was used to test for equivalence of the mean log densities with an equivalency margin of 0.5 log. Minitab v22 was used for statistical analysis and MATLAB R2023a was used for plot generation.

To visualize biofilm one center coupon, wall coupon, and sensor were stained with Syto 9 green-fluorescent nucleic acid stain (0.3 % final concentration) for 30 min and imaged with confocal laser scanning microscopy (CLSM) using a Leica SP8 DIVE (488 nm excitation, 500–550 nm emission). Image Z-stacks were collected in 1 μm steps. The 3D structure was reconstructed from the CLSM images using IMARIS software (9.8).

2.6. Temperature data collection

Temperature sensors in the coupon ring of the SMBR were connected via the electrical slip ring to a Keithley DAQ6510 Data Acquisition/Multimeter System with a Keithley 7711 Multiplexor card and programmed to log two-wire resistance measurements every 30 min. Following the completion of the experiment, the resistance data were transformed into temperature values using the thermal coefficient of resistance and reference resistances of the sensors previously measured ($T = T_{ref} + 1/\mathrm{TCR} * ((R - R_{ref})/R_{ref})$). The average temperature recorded by the microfabricated sensors was compared to the ambient air temperature measured every 30 min with a HOBO MX100 Temperature Data Logger.

3. Results

3.1. CFD simulation

Under steady state conditions, fluid in a cylinder that rotates around its central axis should settle into rigid body motion, where the tangential velocity increases linearly with the distance from the central axis ($v_\theta = \omega r$, with the expected velocity at the wall in the SBMR being 90.7 mm/s) and the analytic solution results in zero intra-fluid shearing. However, when simulated as steady, the reactor demonstrated strong, unsteady vortices at the outermost radii of the reactor that transitioned into oscillatory waves between the coupon ring and both endcaps. The solution instability occurred in the fully 3D and ¼ simulations. A similar phenomenon has been observed experimentally with translating bubble rings [36]. Due to these instabilities, an unsteady formulation was necessary.

While the large vortices seen in the steady solutions were no longer observed in the unsteady formulation, the flow in the SMBR developed small-scale velocity perturbations that increased in magnitude with their radial position. Fig. 3 shows the axial component of the velocity within the reactor, where small-scale mixing could be observed in the outer radii. As seen, the axial components of the fluid velocity are quite small and are, on average, 0.17 % of their local tangential components. The maximum absolute error in the tangential velocity component was 0.0467 mm/s from the rigid-body velocity.

Deriving from small-scale velocity perturbations, the volume-weighted average of fluid shear in the SMBR was 0.20 ± 0.15 mPa. A central core existed with the lowest fluid shear of 0.04 mPa that grew nearly linearly to 0.30 mPa at the reactor wall. Shear stresses higher than 1 mPa were only found at the periodic boundaries of the model in 0.7 % of the bulk fluid (Fig. 4). These higher shear stresses were, however, an artifact of the ¼ symmetry reactor model created by introducing false boundaries and are not representative of conditions within the reactor, which remain <1 mPa.

The wall shear stress on the reactor surfaces also remained small (*i.e.*, ≪1 mPa). When the simulation reached a periodically steady solution, the polycarbonate wall, coupons, and sensor surfaces had an average shear stress of 0.29 ± 0.31 mPa, 0.03 ± 0.02 mPa, and 0.02 ± 0.01 mPa, respectively (Fig. 5). Maximum shear stress on the reactor walls, biofilm coupons, and sensor surfaces were 24.9 mPa, 0.17 mPa, and 0.22 mPa, respectively (Fig. 5). Addressing the artificially elevated shear stresses induced by the ¼ symmetry model, the shear stresses on 0.7 % of the reactor's walls were greater than 1 mPa (max. 24.9 mPa) along the introduced symmetry plane of the model. These planes generated artefacts that are not representative of the fluid behavior on the vast majority (99.3 %) of the reactor walls. While it may be anticipated that a dominant shear direction would develop on the surfaces due to the constant rotation, no strong preference was observed on either the sensor or biofilm coupon surfaces.

3.2. Biofilm growth and sensor integration in the SMBR

The average biofilm $\log_{10}$ densities were 6.2, 6.1, and 5.9 CFU/cm^2 for the wall coupons, sensors, and center coupon surfaces, respectively and were significantly statistically different ($p = 0.015$) (Fig. 6). However, after applying an equivalency margin of 0.5 log to account for practical differences between biological replicates [37,38], the detected differences of 0.3 log between locations and surface type were not significant. Biofilms were imaged with confocal microscopy to confirm attachment. Collectively, biofilm developed into dense spherical shapes on the surfaces of the biofilm coupons and sensors (Fig. 7). The bulk concentration following the 24hr incubation in the SMBR was found to be 6.8 ± 0.07 $\log_{10}$ CFU mL^{-1}.

Successful sensor integration was validated by the integrated RTD sensors. The electrical slip ring allowed for uninterrupted, continuous measurements (Supplemental Figure S2). Small diurnal temperature fluctuations in the lab as well as heat capacity differences between the reactor, media, and ambient air contributed to deviations between the RTD sensors and HOBO datalogger.

4. Discussion

A major challenge of the SMBR development was sensor integration. The geometry of commercially available RWVs like the Synthecon RCC and HARV [39], which are standard devices for microbial research in LSMMG, only allow for limited sensor integration at the center of

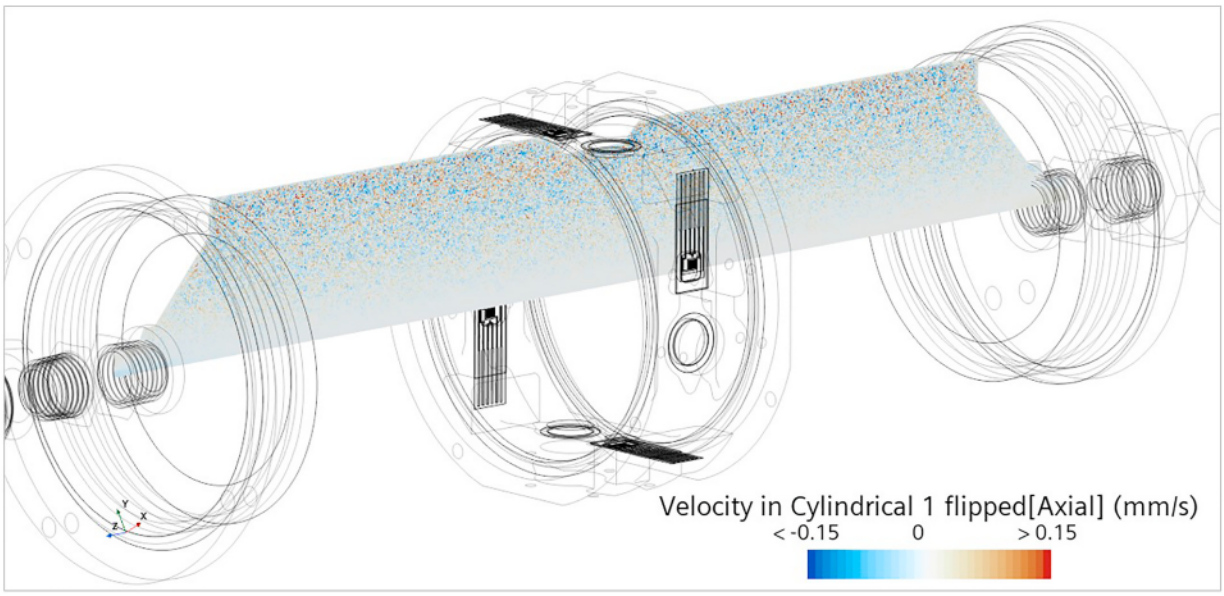

Fig. 3. Output from CFD model overlaid with 3-dimensional outline of the SMBR and the locations of the sensors and biofilm coupons. The axial-component of velocity (positive flow left to right) is shown in a cross-section of the SMBR at 16.9361 s. Small-scale mixing can be seen in the outer radii of the reactor.

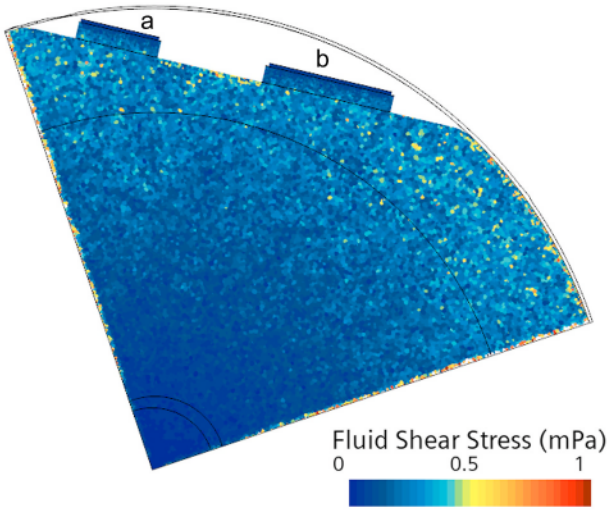

Fig. 4. SMBR Symmetry (¼) CFD model results showing the magnitude of the intra-fluid shear stress (mPa) within the SMBR on a plane across the coupon ring and cutting through the middle of the a) sensor and b) coupon recesses. Shear stress increases from the center of the reactor to the outer radii corresponding with an increase in velocity from the center to the outer wall. Note the increased shear at the symmetry boundaries which are an artifact of the model setup and are not representative of the bulk fluid behavior.

rotation of the reactor [40]. For the integration of many compact commercial electrochemical devices (pH, conductivity, temperature, oxidative redox potential, etc.) that are not probe-type sensors, the optimal location for integration is at the wall of the reactor to protect the circuitry and to allow for uninterrupted electrical connection between the sensor and the measurement device. Integration of sensors in-plane with the wall of the reactor also reduces or eliminates stagnation zones or interruption to the fluid flow. In the present study, a 12-channel electrical slip ring was integrated at the reactor influent to allow for continuous electrical connection during reactor operation, and the successful operation of the slip ring/reactor combination was demonstrated through RTD sensor measurements. While the reactor was developed for biosensors, RTD sensors were integrated to demonstrate proof of concept. Future biosensor integration requires understanding the electrochemical characteristics of a given media [41], which was beyond the scope of this study.

As our reactor design is substantially different from previously simulated designs, fluid modeling was necessary for comparison. LSMMG reactors like the HARV have circular internal cross-sections and well-defined fluid behavior as demonstrated by Masiello et al. and Nauman et al. [25,42]. Of particular interest in LSMMG reactors is the fluid shear stress, as it has been shown to directly affect the behavior of microorganisms [43,44]. A shear stress of 1 mPa was used as the limit for the SMBR CFD models [43,45].

In non-agitated RWVs, deviations from rigid-body behavior resulting in increased fluid shear are the result of the small velocity perturbations described previously. In the SMBR, the wall shear stress on 99.3 % of the reactor surfaces is below 1 mPa, with the average shear stress throughout the bulk media of the reactor being 0.20 mPa. Comparatively, in 10 mL and 50 mL HARV reactors, the maximum wall shear stress was found to be approximately 0.10 mPa and 1.0 mPa, respectively, at a rotation speed of 25 RPM [25,42]. Significantly higher shear (50 mPa–350 mPa) in both the bulk fluid and at the walls has been reported for the random positioning machine, an alternative simulated microgravity reactor that targets only the vector averaging method of simulated microgravity [46]. Caution is advised, however, when comparing shear stress within the SMBR to models of existing LSMMG reactors. Shear stress depends on the mesh resolution generated in the CFD model, and the mesh characteristics at the walls in the previously mentioned CFD models are unknown. Nonetheless, the modelled shear stresses within the SMBR and particularly along the walls were well below the shear stress that defines established LSMMG environments [25,42].

Although the bulk fluid behavior of the SMBR followed the LSMMG behavior depicted in previous CFD models (i.e., approximately rigid body), the cavities of the biofilm coupons and sensors appear to have reduced shear stresses compared to the bulk fluid of the reactor. While flow over cavities can filter eddies reducing the turbulence in the cavity [47], the media in the SMBR is essentially static when analyzed in a rotating reference frame. Therefore, the reduction in fluid shear on the biofilm coupons and sensor surfaces was attributed to local changes in the element size instead of cavity filtering. The mesh elements in these recesses are five times smaller than the elements in the bulk reactor

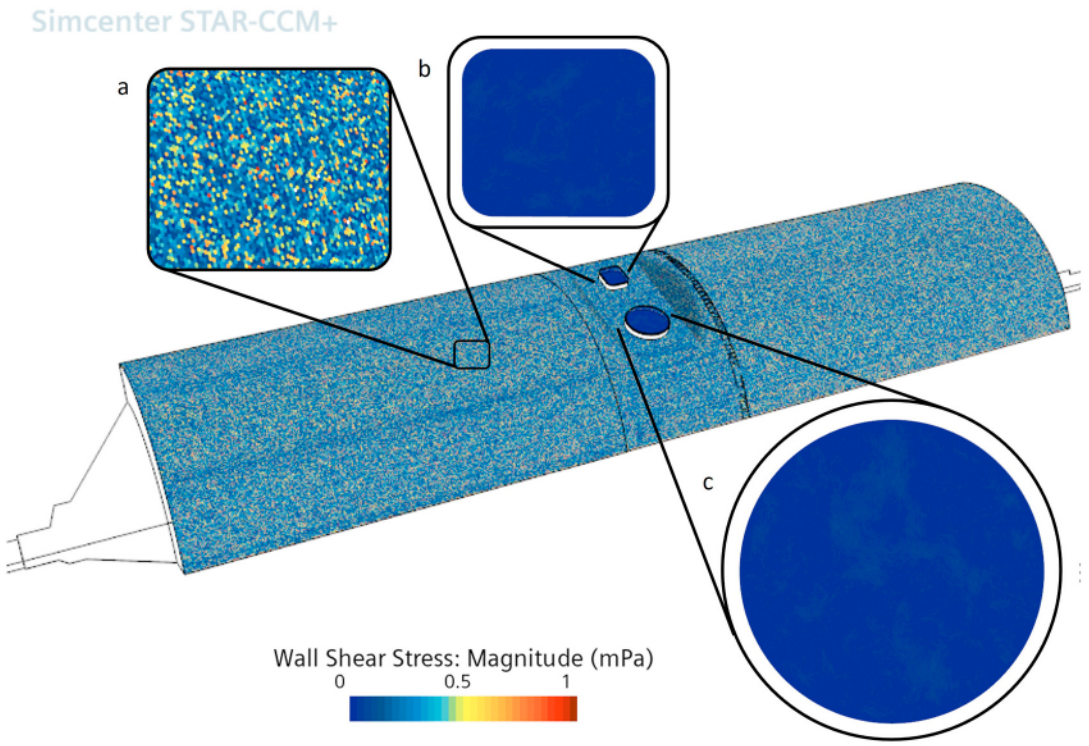

Fig. 5. CFD modelled output of instantaneous wall shear stress on the SMBR wall at 16.9361s. Wall shear stress is shown in detail on the a) polycarbonate reactor wall, b) the sensor surface, and c) the biofilm coupon surface. The area-weighted average wall shear stress for the surfaces were 0.29 ± 0.31 mPa, 0.02 ± 0.01 mPa, 0.03 ± 0.02 mPa, respectively. The difference in the mesh size by location can be seen by comparing image a to images b and c.

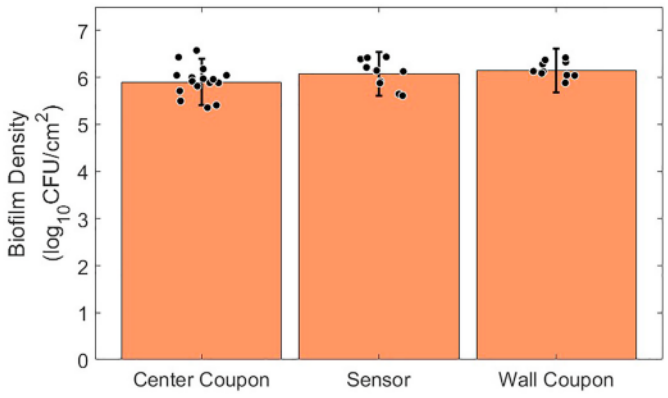

Fig. 6. Biofilm growth on coupons (log10 CFU/cm2) within the SMBR. CFU normalized to surface area for all three locations within the reactor over three experiment replications. A linear mixed effects model was applied to the data with an equivalency margin of 0.5 log. The average $\log_{10}$ CFU/cm^2 of the sampling locations were 5.9, 6.1, and 6.2 for the center coupons, sensors, and wall coupons, respectively. The individual samples are shown in black dots for each sampling location and the standard deviation is indicated.

volume, and the mesh prism layer thickness on the biofilm coupon and sensor surfaces is approximately 10 % of the average element size throughout the reactor. These attributes are the expected source of the roughly one-order-of-magnitude difference in reported shear values between the bulk fluid behavior and the fluid in the recesses. Intra-fluid and wall shear stresses are not a principal variable in CFD. Instead, the simulation solves for the velocity in the mesh elements, and the shear stress is calculated from the change in velocity across the neighboring elements. Following this trajectory, demonstrated by the biofilm coupon and sensor mesh results, the calculated shear stress will converge to an asymptotic value as the element size decreases, which is the solution of the CFD model (Supplemental Figure S4). Similarly, local differences in the maximum shear stress on the polycarbonate wall, biofilm coupons, and sensor surfaces are best explained by element size (Fig. 4).

The continuous low shear environment that was achieved in the SMBR allowed for the development of microbial biofilms at different locations in the reactor. Biofilm enumerated on the coupon and sensor surfaces were not statistically different between the locations (Fig. 6). CLSM images of biofilm on all test surfaces showed the attachment of spherical bacterial colonies (Fig. 7). If the center and wall environments in the reactor had differed, as is commonly found for coupons in the Center for Disease Control Biofilm Reactor, we would expect to see either differences in cellular attachment, morphology or both, due to differences in fluid behavior [38,48]. Spherical biofilm morphology has previously been shown for eukaryotic cells grown under simulated microgravity [49] and is an expected behavior for cellular aggregates in RWVs [42]. Visualization of bacterial cell aggregates during additional SMBR experiments also supported these morphological changes from initial undefined cell clusters in the inoculum to spheroids in the bulk effluent fluid after 24 h (Supplemental Figure S3). While there has been limited biofilm research conducted in actual microgravity conditions (e.g. on the ISS and space shuttles), one study described biofilm in a unique column-and-canopy growth morphology with spheroid-like growth on the surface forming the columns and a bacterial mat canopy following incubation at 37 °C for 72 h [11]. The bacterial spheroids generated in the present study could be the foundation of this unique morphology, but longer experiments are needed to better understand if this can be replicated in LSMMG.

Sampling of biofilm reactors repeatedly over time has posed significant challenges. To maintain a stable fluid environment in RWVs the reactor cannot be stopped until the end of the experiment, which has limited temporal sampling to the bulk media effluent. Previous biofilm studies in LSSMG have looked at biofilm formation on gas exchange membranes, glass beads, and cells aggregates formed in the bulk fluid in a HARV [24,44], but these methods are also limited to bulk and

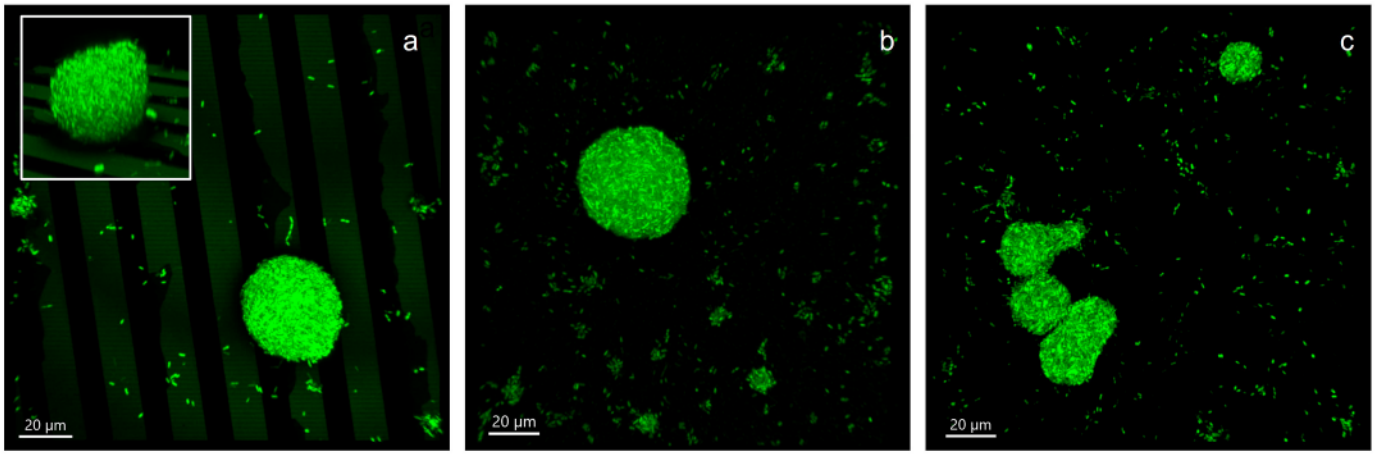

Fig. 7. Biofilm growth in the SMBR. Confocal laser scanning microscopy images captured using a Leica SP8 DIVE from a) microfabricated sensor surface with gold electrodes visible (inset depicts side profile of spheroid), b) coupon ring biofilm coupon, and c) center biofilm coupon. Cells are stained with green-fluorescent nucleic acid stain, Syto 9. Biofilm accumulation on all three surfaces took the form of spherical cell clusters. Scale bars are 20 µm. (For interpretation of the references to colour in this figure legend, the reader is referred to the Web version of this article.)

endpoint sampling. The integration of biosensors and biofilm coupons within a RWV addresses this challenge and provides information about biofilm development and accumulation during reactor operation.

5. Conclusions

While previous models suggest that the reactor wall should be ignored in LSMMG simulations due to hypothesized greater stresses on the particles and poor mass transport [23,42,50], both the CFD model and CFU enumeration in this study demonstrate that the fluid environment at the walls does not differ significantly from the bulk fluid and can serve as a representative surface for biofilm behavior in LSMMG. The CFD analysis indicated very low shear throughout the reactor allowing for a continuation of the LSMMG model from the center of the reactor to the walls, where biofilm accumulation can be expected. The SMBR also has a much larger volume than commercially available reactors, which is beneficial for experiments that aim to understand flow in a more realistic pipe environment in spacecraft. Through this study, it was shown that custom microfabricated sensor data collection is continuous, reliable and agrees with commercial sensors. Future work will continue modeling the fluid environment within the SMBR, exploring microbial detection with microfabricated biosensors, and optimizing rotation speeds for longer experiments. The successful integration of microfabricated sensors into an RWV is crucial towards understanding biofilm dynamics in microgravity environments.

CRediT authorship contribution statement

Haley M. Ketteler: Writing – original draft, Visualization, Methodology, Investigation, Formal analysis, Data curation, Conceptualization. **Erick L. Johnson:** Writing – original draft, Visualization, Methodology, Investigation, Formal analysis, Data curation, Conceptualization. **Matthew McGlennen:** Writing – review & editing, Methodology, Data curation, Conceptualization. **Markus Dieser:** Writing – review & editing, Methodology, Formal analysis, Conceptualization. **Christine M. Foreman:** Writing – review & editing, Supervision, Methodology, Funding acquisition, Conceptualization. **Stephan Warnat:** Writing – review & editing, Supervision, Methodology, Funding acquisition, Conceptualization.

Declaration of competing interest

The authors declare the following financial interests/personal relationships which may be considered as potential competing interests: Stephan Warnat reports financial support was provided by NASA. Christine M. Foreman reports financial support was provided by NASA. If there are other authors, they declare that they have no known competing financial interests or personal relationships that could have appeared to influence the work reported in this paper.

Acknowledgments

Thank you to Elizabeth L. Sandvik for providing the *Ralstonia insidiosa* strain and FlowCam sample processing assistance and Albert Parker for assistance with the statistical analysis of the data. This work was performed in part at the Montana Nanotechnology Facility, a member of the National Nanotechnology Coordinated Infrastructure (NNCI), which is supported by the National Science Foundation (Grant# ECCS1542210), and the Center for Biofilm Engineering, both at Montana State University. This work was supported by NASA EPSCoR grant #80NSSC20P0581 to CMF and SW and NASA CAN grant #80NSSC20M0246 to CMF and SW. This work was supported by a NASA Space Technology Graduate Research Opportunity to HMK and CMF. Imaging was made possible by the Center for Biofilm Engineering Imaging Facility at Montana State University, which is supported by funding from the National Science Foundation MRI Program (2018562), the M. J. Murdock Charitable Trust (202016116), and the US Department of Defense (77369LSRIP).

Appendix ASupplementary data

Supplementary data to this article can be found online at https://doi.org/10.1016/j.bioflm.2025.100263.

Data availability

Data will be made available on request.

References

[1] Donlan RM, Costerton JW. Biofilms: survival mechanisms of clinically relevant microorganisms. Clin Microbiol Rev 2002;15(2):167–93. https://doi.org/10.1128/cmr.15.2.167-193.2002.
[2] Klintworth R, Reher HJ, Viktorov AN, Bohle D. Biological induced corrosion of materials II: new test methods and experiences from mir station. Acta Astronaut 1999;44(7):569–78. https://doi.org/10.1016/S0094-5765(99)00069-7.
[3] Vaishampayan A, Grohmann E. Multi-resistant biofilm-forming pathogens on the international space station. J Biosci 2019;44(5). https://doi.org/10.1007/s12038-019-9929-8.

[4] Weir N, Wilson M, Yoets A, Molina T, Bruce R, Carter L. *Microbiological Characterization of the international space station water processor assembly external filter assembly S/N 01* 42nd international conference on environmental systems 2012, ICES 2012. 2012, 07.

[5] Bruce RJ, Ott CM, Skuratov VM, Pierson DL. Microbial surveillance of potable water sources of the international space station. SAE Trans 2005;114:283–92. http://www.jstor.org/stable/44682723.

[6] Velez Justiniano Y-A, Carter DL, Nur M, Angle G. *Developing Methods for biofilm Control in Microgravity for a water recovery system* 2020 international conference on environmental systems. Virtual; 2020, July 31, 2020.

[7] Albrecht-Buehler G. The simulation of microgravity conditions on the ground. ASGSB Bull 1992;5(2):3–10.

[8] Klaus DM. Clinostats and bioreactors. Gravitational and Space Research 2001;14 (2):55–64.

[9] Aunins TR, Erickson KE, Prasad N, Levy SE, Jones A, Shrestha S, Mastracchio R, Stodieck L, Klaus D, Zea L, Chatterjee A. Spaceflight modifies Escherichia coli gene expression in response to antibiotic exposure and reveals role of oxidative stress response [original research]. Front Microbiol 2018;9. https://doi.org/10.3389/fmicb.2018.00310.

[10] Crabbé A, Schurr MJ, Monsieurs P, Morici L, Schurr J, Wilson JW, Ott CM, Tsaprailis G, Pierson DL, Stefanyshyn-Piper H, Nickerson CA. Transcriptional and proteomic responses of *Pseudomonas aeruginosa* PAO1 to spaceflight conditions involve hfq regulation and reveal a role for oxygen. Appl Environ Microbiol 2011; 77(4):1221–30. https://doi.org/10.1128/AEM.01582-10.

[11] Kim W, Tengra FK, Young Z, Shong J, Marchand N, Chan HK, Pangule RC, Parra M, Dordick JS, Plawsky JL, Collins CH. Spaceflight promotes biofilm formation by Pseudomonas aeruginosa. PLoS One 2013;8(4):e62437. https://doi.org/10.1371/journal.pone.0062437.

[12] Mclean RJC, Cassanto JM, Barnes MB, Koo JH. Bacterial biofilm formation under microgravity conditions. FEMS (Fed Eur Microbiol Soc) Microbiol Lett 2001;195 (2):115–9. https://doi.org/10.1111/j.1574-6968.2001.tb10507.x.

[13] Schiwon K, Arends K, Rogowski KM, Fürch S, Prescha K, Sakinc T, Van Houdt R, Werner G, Grohmann E. Comparison of antibiotic resistance, biofilm formation and conjugative transfer of Staphylococcus and Enterococcus isolates from international space station and antarctic research station concordia. Microb Ecol 2013;65(3):638–51. https://doi.org/10.1007/s00248-013-0193-4.

[14] Singh NK, Wood JM, Karouia F, Venkateswaran K. Succession and persistence of microbial communities and antimicrobial resistance genes associated with International Space Station environmental surfaces. Microbiome 2018;6(1). https://doi.org/10.1186/s40168-018-0585-2.

[15] Zea L, Larsen M, Estante F, Qvortrup K, Moeller R, Oliveira SDd, Stodieck L, Klaus D. Phenotypic changes exhibited by E. coli cultured in space. Front Microbiol 2017;8.

[16] Sobisch L-Y, Rogowski KM, Fuchs J, Schmieder W, Vaishampayan A, Oles P, Novikova N, Grohmann E. Biofilm forming antibiotic resistant gram-positive pathogens isolated from surfaces on the international space station [original research]. Front Microbiol 2019;10. https://doi.org/10.3389/fmicb.2019.00543.

[17] Hammond TG, Hammond JM. Optimized suspension culture: the rotating-wall vessel. Am J Physiol Ren Physiol 2001;281(1):F12–25. https://doi.org/10.1152/ajprenal.2001.281.1.f12.

[18] Klaus DM, Todd P, Schatz A. Functional weightlessness during clinorotation of cell suspensions. Adv Space Res 1998;21(8–9):1315–8. https://doi.org/10.1016/s0273-1177(97)00404-3.

[19] Nickerson CA, Ott CM, Wilson JW, Ramamurthy R, Pierson DL. Microbial responses to microgravity and other low-shear environments. Microbiol Mol Biol Rev 2004; 68(2):345–61. https://doi.org/10.1128/mmbr.68.2.345-361.2004.

[20] Wolf DA, Schwarz RP. Analysis of gravity-induced particle motion and fluid perfusion flow in the NASA-designed rotating zero-head-space tissue culture vessel. National Aeronautics and Space Administration; 1991. Retrieved from, https://ntrs.nasa.gov/citations/19920004122.

[21] Goodwin TJ, Prewett TL, Wolf DA, Spaulding GF. Reduced shear stress: a major component in the ability of mammalian tissues to form three-dimensional assemblies in simulated microgravity. J Cell Biochem 1993;51(730):301–11. 2312 (Print).

[22] Thomas WE, Trintchina E, Forero M, Vogel V, Sokurenko EV. Bacterial adhesion to target cells enhanced by shear force. Cell 2002;109(7):913–23. https://doi.org/10.1016/s0092-8674(02)00796-1.

[23] Begley CM, Kleis SJ. The fluid dynamic and shear environment in the NASA/JSC rotating-wall perfused-vessel bioreactor. Biotechnol Bioeng 2000;70(1):8. https://doi.org/10.1002/1097-0290(20001005)70:1.

[24] Lynch SV, Mukundakrishnan K, Benoit MR, Ayyaswamy PS, Matin A. Escherichia coli biofilms formed under low-shear modeled microgravity in a ground-based system. Appl Environ Microbiol 2006;72(12):7701–10. https://doi.org/10.1128/AEM.01294-06.

[25] Nauman EA, Ott CM, Sander E, Tucker DL, Pierson D, Wilson JW, Nickerson CA. Novel quantitative biosystem for modeling physiological fluid shear stress on cells. Appl Environ Microbiol 2007;73(3):699–705. https://doi.org/10.1128/aem.02428-06.

[26] Allen LA, Kalani AH, Estante F, Rosengren AJ, Stodieck L, Klaus D, Zea L. Simulated micro-, lunar, and martian gravities on earth—effects on Escherichia coli growth, phenotype, and sensitivity to antibiotics. Life 2022;12.

[27] Liu T, Li X, Sun X, Ma X, Cui Z. Analysis on forces and movement of cultivated particles in a rotating wall vessel bioreactor. Biochem Eng J 2004;18(2):97–104. https://doi.org/10.1016/S1369-703X(03)00171-2.

[28] Castro VA, Thrasher AN, Healy M, Ott CM, Pierson DL. Microbial characterization during the early habitation of the international space station. Microb Ecol 2004;47 (2):119–26. https://doi.org/10.1007/s00248-003-1030-y.

[29] Conde A. 2020 NASA technology taxonomy. Retrieved 13 April 2023 from, https://www.nasa.gov/offices/oct/taxonomy/index.html; 2020.

[30] Højris B, Christensen SCB, Albrechtsen H-J, Smith C, Dahlqvist M. A novel, optical, on-line bacteria sensor for monitoring drinking water quality. Sci Rep 2016;6(1): 23935. https://doi.org/10.1038/srep23935.

[31] McGlennen M, Dieser M, Foreman CM, Warnat S. Using electrochemical impedance spectroscopy to study biofilm growth in a 3D-printed flow cell system. Biosens Bioelectron X 2023;14:100326. https://doi.org/10.1016/j.biosx.2023.100326.

[32] Wang L, Wang R, Chen F, Jiang T, Wang H, Slavik M, Wei H, Li Y. QCM-based aptamer selection and detection of Salmonella typhimurium. Food Chem 2017; 221:776–82. https://doi.org/10.1016/j.foodchem.2016.11.104.

[33] Drescher K, Shen Y, Bassler BL, Stone HA. Biofilm streamers cause catastrophic disruption of flow with consequences for environmental and medical systems. Proc Natl Acad Sci USA 2013;110(11):4345–50. https://doi.org/10.1073/pnas.1300321110.

[34] Singh H, Hutmacher DW. Bioreactor studies and computational fluid dynamics. In: Bioreactor systems for tissue engineering. Springer Berlin Heidelberg; 2009. p. 231–49. https://doi.org/10.1007/10_2008_6.

[35] Velez Justiniano Y-A, Carter DL, Sandvik E, Stewart PS, Goeres DM, Sturman PJ, Li W, Johnson A, Cioanta J. Biofilm management in a microgravity water recovery system. 50th international conference on environmental systems. 2021, 12 July 2021.

[36] Seiden G, Ungarish M, Lipson SG. Banding of suspended particles in a rotating fluid-filled horizontal cylinder. Phys Rev 2005;72(2). https://doi.org/10.1103/physreve.72.021407.

[37] ASTM. Standard practices for evaluation of inactivators of antimicrobial agents 2022;E1054–22.

[38] Buckner E, Buckingham-Meyer K, Miller LA, Parker AE, Jones CJ, Goeres DM. Coupon position does not affect Pseudomonas aeruginosa and Staphylococcus aureus biofilm densities in the CDC biofilm reactor. J Microbiol Methods 2024;223: 106960. https://doi.org/10.1016/j.mimet.2024.106960.

[39] Synthecon I. 3D cell culture bioreactors - rotary cell culture. https://synthecon.com/pages/rotary_cell_culture_systems_13.asp; 2024.

[40] Saarinen MA, Reece JS, Arnold MA, Murhammer DW. Monitoring and controlling the dissolved oxygen (DO) concentration within the high aspect ratio vessel (HARV). Biotechnol Prog 2008;19(4):1335–41. https://doi.org/10.1021/bp0257574.

[41] McGlennen M, Dieser M, Foreman CM, Warnat S. Monitoring biofilm growth and dispersal in real-time with impedance biosensors. J Ind Microbiol Biotechnol 2023; 50(1). https://doi.org/10.1093/jimb/kuad022.

[42] Masiello T, Dhall A, Hemachandra M, Tokranova N, Melendez J, Castracane J. Analyzing fluid shear stress in the RCCS: applications for 3D cell culture. In: *Simulated microgravity* COMSOL conference; 2018, 7 November 2018. Boston, MA.

[43] Chun ALM, Mosayyebi A, Butt A, Carugo D, Salta M. Early biofilm and streamer formation is mediated by wall shear stress and surface wettability: a multifactorial microfluidic study. MicrobiologyOpen 2022;11(4). https://doi.org/10.1002/mbo3.1310.

[44] Crabbé A, De Boever P, Van Houdt R, Moors H, Mergeay M, Cornelis P. Use of the rotating wall vessel technology to study the effect of shear stress on growth behaviour of*Pseudomonas aeruginosa*PA01. Environ Microbiol 2008;10(8): 2098–110. https://doi.org/10.1111/j.1462-2920.2008.01631.x.

[45] Nguyen AV, Shourabi AY, Yaghoobi M, Zhang S, Simpson KW, Abbaspourrad A. A high-throughput integrated biofilm-on-a-chip platform for the investigation of combinatory physicochemical responses to chemical and fluid shear stress. PLoS One 2022;17(8):e0272294. https://doi.org/10.1371/journal.pone.0272294.

[46] Wuest SL, Stern P, Casartelli E, Egli M. Fluid dynamics appearing during simulated microgravity using random positioning machines. PLoS One 2017;12(1):e0170826. https://doi.org/10.1371/journal.pone.0170826.

[47] Nallasamy M, Prasad KK. On cavity flow at high Reynolds numbers. J Fluid Mech 1977;79(2):391–414. https://doi.org/10.1017/S0022112077000214.

[48] Johnson E, Petersen T, Goeres DM. Characterizing the shearing stresses within the CDC biofilm reactor using computational fluid dynamics. Microorganisms 2021;9 (8):1709. https://doi.org/10.3390/microorganisms9081709.

[49] Brown LA, Arterburn LM, Miller AP, Cowger NL, Hartley SM, Andrews A, Silber PM, Li AP. Maintenance of liver functions in rat hepatocytes cultured as spheroids in a rotating wall vessel. In: cellular & developmental biology. Animal, vol. 39; 2003.

[50] Ayyaswamy PS, Mukundakrishnan K. Optimal conditions for simulating microgravity employing NASA designed rotating wall vessels. Acta Astronaut 2007;60(4):397–405. https://doi.org/10.1016/j.actaastro.2006.09.008.